Journal Pre-proof

Modulus spectroscopy for the detection of parallel electric responses in electroceramics

Till Frömling, Yao Liu, An-Phuc Hoang, Maximillian Gehringer, Sebastian Steiner, Mikalai Zhuk, Julia Glaum, Bai-Xiang Xu

PII: S2352-8478(21)00177-5

DOI: https://doi.org/10.1016/j.jmat.2021.12.005

Reference: JMAT 527

To appear in: *Journal of Materiomics*

Received Date: 5 August 2021

Revised Date: 12 December 2021

Accepted Date: 20 December 2021

Please cite this article as: Frömling T, Liu Y, Hoang A-P, Gehringer M, Steiner S, Zhuk M, Glaum J, Xu B-X, Modulus spectroscopy for the detection of parallel electric responses in electroceramics, *Journal of Materiomics*, https://doi.org/10.1016/j.jmat.2021.12.005.

Modulus spectroscopy for the detection of parallel electric responses in electroceramics

Till Frömling[a,*], Yao Liu[b], An-Phuc Hoang[a], Maximillian Gehringer[a], Sebastian Steiner[a], Mikalai Zhuk[c], Julia Glaum[c], Bai-Xiang Xu[b]

a. Department of Materials and Earth Science, Technical University of Darmstadt, FG Nichtmetallisch-Anorganische Werkstoffe, Alarich-Weiss-Straße 2, 64287 Darmstadt, Germany. Email: froemling@ceramics.tu-darmstadt.de

b. Department of Materials and Earth Science, Technical University of Darmstadt, FG Mechanics of Functional Materials, Otto-Berndt-Straße 3, 64287 Darmstadt, Germany.

c. Department of Materials Science and Engineering, Norwegian University of Science and Technology (NTNU), Functional Materials and Materials Chemistry group (FACET), Sem Sælands vei 12, 7491 Trondheim, Norway

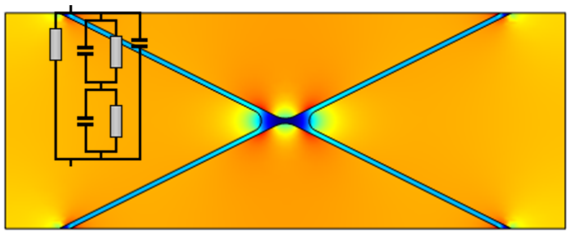

Grain boundary

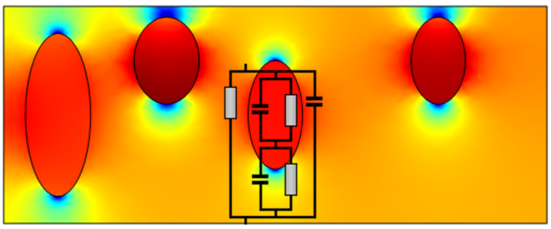

Inclusion

Modulus spectroscopy for the detection of parallel electric responses in electroceramics

Till Frömling[a,*], Yao Liu[b], An-Phuc Hoang[a], Maximillian Gehringer[a], Sebastian Steiner[a], Mikalai Zhuk[c], Julia Glaum[c], Bai-Xiang Xu[b]

a. Department of Materials and Earth Science, Technical University of Darmstadt, FG Nichtmetallisch-Anorganische Werkstoffe, Alarich-Weiss-Straße 2, 64287 Darmstadt, Germany. Email: froemling@ceramics.tu-darmstadt.de

b. Department of Materials and Earth Science, Technical University of Darmstadt, FG Mechanics of Functional Materials, Otto-Berndt-Straße 3, 64287 Darmstadt, Germany.

c. Department of Materials Science and Engineering, Norwegian University of Science and Technology (NTNU), Functional Materials and Materials Chemistry group (FACET), Sem Sælands vei 12, 7491 Trondheim, Norway

Abstract

Impedance spectroscopy has become one of the most versatile and essential investigation methods concerning electrical properties of materials for electronic and energy applications. Deriving knowledge about physical mechanisms, however, often demands excellent expertise in evaluating the spectra. Investigating different representations of the same data set can help elucidate the underlying physics, but this is rarely applied. In this work, the importance of using the modulus representation to identify parallel electric responses is rationalized. Those responses result from parallel conducting pathways, e.g., at grain boundaries, or from regions with differing permittivity, e.g., in composites. Qualitative and quantitative data can be obtained, as it is illustrated based on experimental data from electroceramics and respective physical simulation results using the finite element method. The findings should help to study intricate electric responses of materials with chemical or structural heterogeneity.

1. Introduction

The fast and reliable analysis of materials for energy applications like batteries and fuel cells or electrical components like capacitors and resistors is a major challenge. Usually, the in-depth information obtained from an analysis is rather inversely proportional to its duration [1]. The components' high complexity requires extensive measurements to determine the physical mechanisms leading to changes in functional properties. Even for a comparably simple ceramic capacitor electrode, bulk and grain boundary make distinct contributions to the overall electrical response, and differentiating their effects is challenging [2-5].

One of the best non-destructive methods to obtain information on different parts of a component's respective electrical properties is frequency-dependent impedance spectroscopy [6-14]. In the case of different time constants of the electrical responses, these can be separated and attributed to the responsible physical mechanism. It has been applied to investigate oxygen [15-17] and proton-conducting [18] compounds, electronically conductive materials [4, 5], or mixed electronic/ionic conductors [19-22], and even complete devices like batteries [23, 24]. The measurement itself can be very conveniently conducted. Equipment for the analysis in wide frequency ranges to elucidate dielectric and conductive responses is generally available and not expensive. Therefore, impedance data can be quite easily obtained. Over the last decades, it has been shown that impedance spectroscopy is one of the most important tools for analyzing materials for electronic and energy applications.

As good as this sounds, there is, of course, a catch. The obtained data is often difficult to interpret [14]. Depending on the system, sufficient experience is needed to interpret the data with the underlying physical mechanisms, and there could be multiple interpretations for the same set of data. Even if the evaluation is done expertly, the full potential is often not exploited. The key to obtaining the most and best information from impedance spectroscopy is the examination of many, if not all, possible representations of the data [9, 10, 25, 26].

The necessity of revisiting the interpretation of electrical responses of materials resulted in our case from investigations of new ferroelectric or dielectric materials derived from lead-free ceramic compositions [27, 28]. These can be structurally and chemically very complex and can even form composites during regular solid-state synthesis [29, 30]. For example, solid solutions based on $Na_{1/2}Bi_{1/2}TiO_3$ (NBT) are often relaxor ceramics [31]. This means that they contain small polarizable regions, so-called polar nano-regions (PNR), which only under certain conditions, e.g., applied electric field, form correlated ferroelectric domains [32, 33]. They do not undergo a clearly defined phase transition with temperature. It is hypothesized that it instead changes its content of particular PNR (low temperature (LT) and high temperature (HT) PNR) with temperature [34]. This results in a phase coexistence regime of PNR with rhombohedral and tetragonal structures [35, 36]. Furthermore, a very

broad transition peak in the permittivity can be determined as in Figure 1a (blue line) for NBT and solid solutions of NBT with barium titanate (NBT-BT). This broadened peak can be further disrupted by increasing the disorder through the formation of solid solutions with additional components like calcium zirconate (CZ) or $K_{0.5}Na_{0.5}NbO_3$ (KNN). This is illustrated by the schematic red plot in Figure 1a [37]. A lower but temperature stable permittivity is induced, which makes the material interesting for high-temperature capacitors [34, 37-39]. In the previous works in which this material was investigated, modulus plots were discussed, as well [34, 37]. These are depicted in Figure 1b for various CZ content. The imaginary part of the modulus M'' shows two separate responses when plotted against the frequency. The low-frequency peak has a higher M'' than the high-frequency peak (shoulder in Figure 1b). If the bricklayer model (Fig. 2) was applied, that would mean a low conductivity region with low capacitance ($M''_{max} = \frac{\varepsilon_0 * A/d}{2C} = \frac{C_0}{2C}$) in series to a high conductivity region with high capacitance [2, 3]. This seems very odd as we would usually expect that a conductive response does not result in high capacitances. For a high capacitance to occur, a charge built-up should be possible, but that is mutually exclusive with high conductivity. Furthermore, a second process is also not visible in the Nyquist plot in Figure 1c. Thus, the second response would not have been detected if only this plot had been evaluated. The only way this is physically possible using the bricklayer model is if the grain boundary has a higher resistivity/lower conductivity, but its overall contribution to the resistance is lower than the bulk because there is much less grain boundary volume. In this case, a lower resistance for the grain boundary process is measured together with a higher capacitance than the bulk [40]. Nevertheless, it is possible that the dielectric responses of the polar nano-regions contribute to the overall response, as well. For example, as a parallel dielectric contribution. Therefore, it is necessary to re-evaluate the interpretations to rationalize the involved responses.

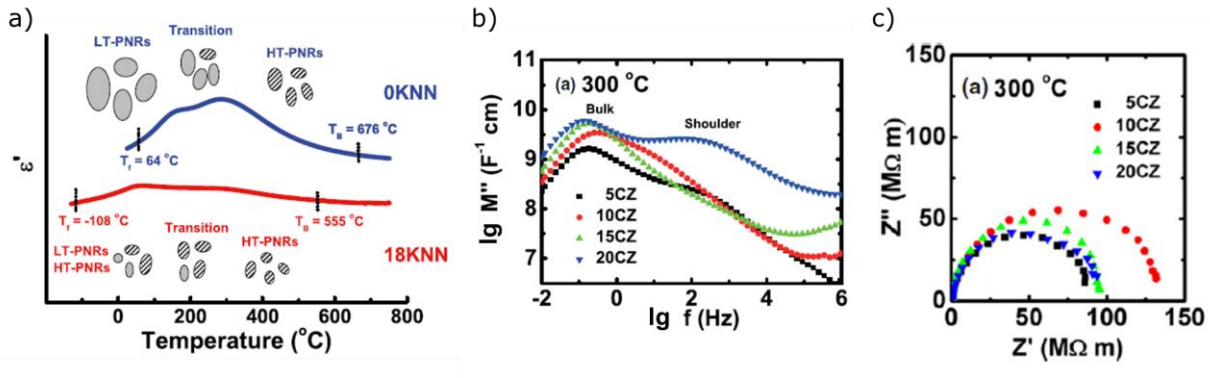

Fig. 1: a) Schematic temperature dependence of ε' for NBT-BT (blue) and NBT-6BT and NBT-6BT-18KNN (red); illustration of the transition from low-temperature to high temperature PNR.[34] b) Modulus at 300°C for NBT-6BT compositions with varying CZ content (5%-20%). c) Nyquist-plot corresponding to the modulus data in b [37]. Copyright, The American Ceramic Society. Reprinted with permission.

1.1. Introduction to different representations of results from impedance spectroscopy

Electrolytes for solid oxide fuel cells or solid-state lithium-ion batteries require high ionic conductivity at either moderate or, in the case of batteries, room temperature. The plots which are analyzed are usually Nyquist-plots (imaginary part of impedance Z'' against the real part Z' (Figure 2a)) and Bode-plots (Z' and Z'' against frequency f (Figure 2d) or conductivity σ against f (Figure 2f)). A charge transport process involves the resistance against the transport and additional charge separation (e.g., charge built up at an electrode)[9]. Thus, the electrical response can often be described by an equivalent circuit with a resistance R and a capacitor C in parallel [14].

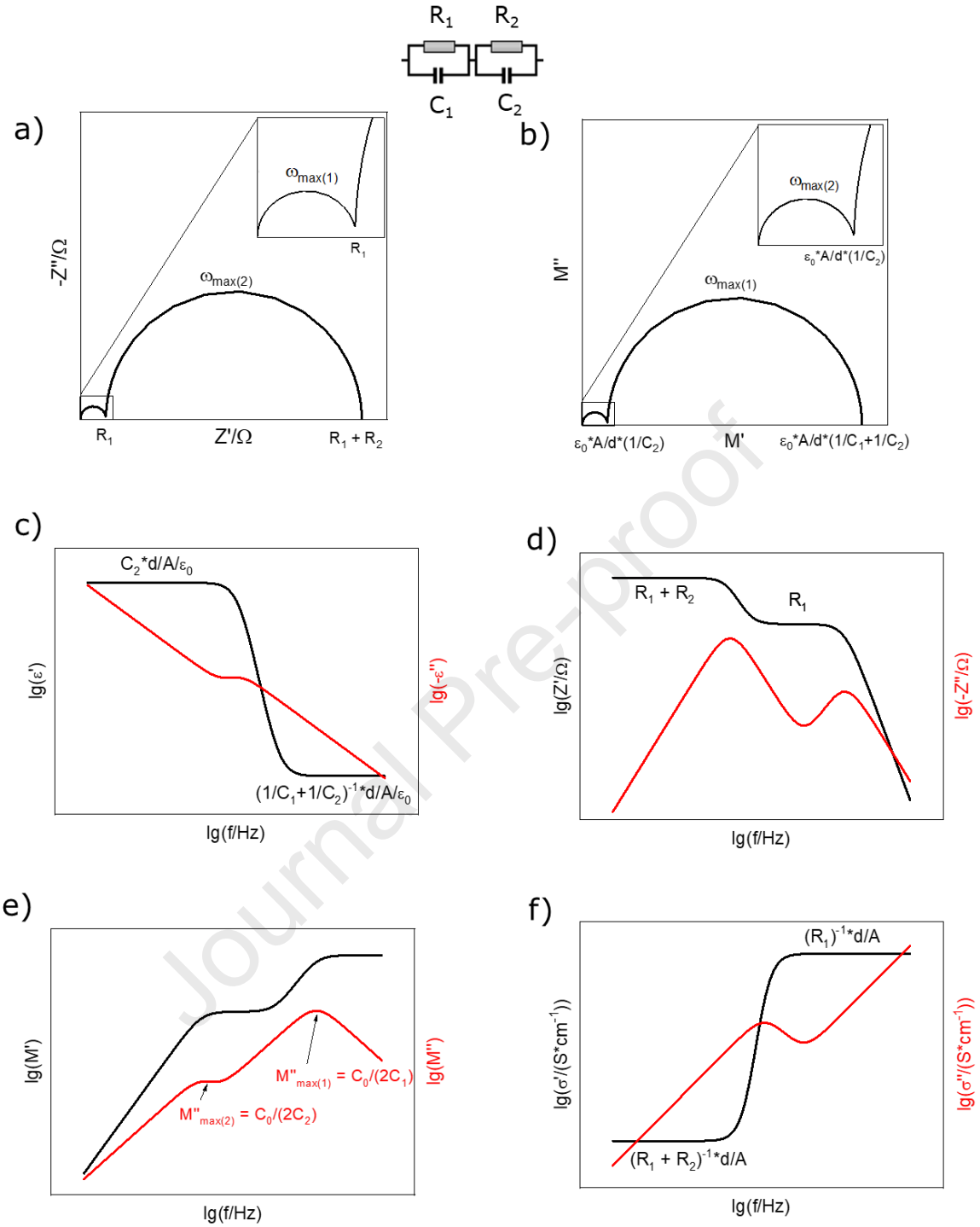

Fig. 2: Schematic illustration of a frequency dependent response of an RC-RC circuit with $C_1 << C_2$ and $R_1 << R_2$ a) Nyquist-plot b) Modulus plot c) Permittivity plotted against frequency d) Impedance plotted against frequency e) Modulus plotted against frequency (with $C_0 = \varepsilon_0 * \frac{d}{A}$) f) Conductivity plotted against frequency.

A grain response and a resistive grain boundary response are considered to be connected in series according to the bricklayer model (Figure 2) [2, 3]. This model describes, e.g., the response of a polycrystalline system in which the grain boundaries are more resistive (and have a higher capacitance) than the bulk. Thus, the responses can be considered serially connected. Such a kind of model is very common for electroceramics. With differences in the time constant τ or angular relaxation frequency

$\omega_{max} = \frac{1}{\tau} = \frac{1}{R \cdot C}$ the two physical mechanisms can be separated. Thus, the resistances of the processes can be obtained from the x-axis interceptions of the semi-circles in Nyquist-plots (Figure 2a) or from the plateaus in Bode-plots of σ' and Z' (Figures 2d and f). Furthermore, the capacitance can be easily derived from a Nyquist-plot with the knowledge of ω_{max} of the respective semi-circle. However, a scientist investigating capacitor or ferroelectric ceramics will mostly be interested in the dielectric response, hence capacitance/permittivity and dielectric loss. Thus, plots of frequency dependent permittivity, where the real component $\varepsilon'$and the imaginary component ε'' of the permittivity are plotted against frequency, can be used to obtain the respective information (Figure 2c).

The determination of the capacitive and resistive behavior is usually conducted with the same measurement approach, but a different representation of the data is used. However, some information may be lost if the focus is only on the parameters of primary interest. For example, it is difficult to obtain information on conductivity contributing to the dielectric loss if only the permittivity representation is used. Therefore, it can be of great help to have a look at the other corresponding representations. These can be obtained from the complex impedance Z^* with the following relations [9, 14]:

$$\sigma^* = \frac{1}{Z^*} \cdot \frac{d}{A} \tag{1}$$

$$\varepsilon^* = \frac{1}{j\omega\varepsilon_0 Z^*} \cdot \frac{d}{A} \tag{2}$$

$$M^* = \frac{1}{\varepsilon^*} = j\omega\varepsilon_0 Z^* \cdot \frac{A}{d} \tag{3}$$

where σ^*, ε^* , and M^* stand for the complex conductivity, permittivity, and modulus, respectively. A is the area of the electrode, *d* the distance between the electrodes, and ε_0 the vacuum permittivity.

The data is essentially the same, but certain properties of the contributing electrical responses are highlighted for each of these representations. The modulus is the least known and has hardly been used for the evaluation of impedance data. In fact, compared to the impedance, the modulus highlights different frequency regions. For example, in Figure 2b, the large semicircle belongs to the high-frequency response and hence the process with low capacitance and resistance. The opposite is the case for the impedance in Figure 2a. Information on the capacitance can also be directly obtained from plotting M'' against the frequency (Figures 2e) without employing a fit using an equivalent circuit. Therefore, this representation has been promoted by Sinclair and co-workers [10, 25, 41]. Additionally, it is possible to elucidate whether a process is a dielectric one (polarization of the material; short-range charge displacement) or can be attributed to long-range charge transport [42]. For example, in the case of a pure dielectric Debye response, we can describe the permittivity with the following equation:

$$\varepsilon^* = \varepsilon_\infty + \left[\frac{\varepsilon_s - \varepsilon_\infty}{1 + j\omega\tau}\right] \tag{4}$$

where ε_∞ is the high-frequency limit of permittivity and ε_s the low-frequency permittivity of the Debye process. Plotting the permittivity against frequency, a similar behavior, as in Figure 2c, is observed. However, only one physical mechanism is responsible for the two plateaus. The transition from ε_s to ε_∞ occurs at $\tau = \omega^{-1}$. As a result of the Debye response, the peak frequencies of the imaginary parts for the different physical quantities may differ significantly depending on $r = \frac{\varepsilon_s}{\varepsilon_\infty}$ (Figure 3a). For high r there is a large separation in the peak position, while for $r \approx 1$ the plots converge. The latter is the case for a purely conductive process. Therefore, a judgment on what kind of process is investigated is possible.

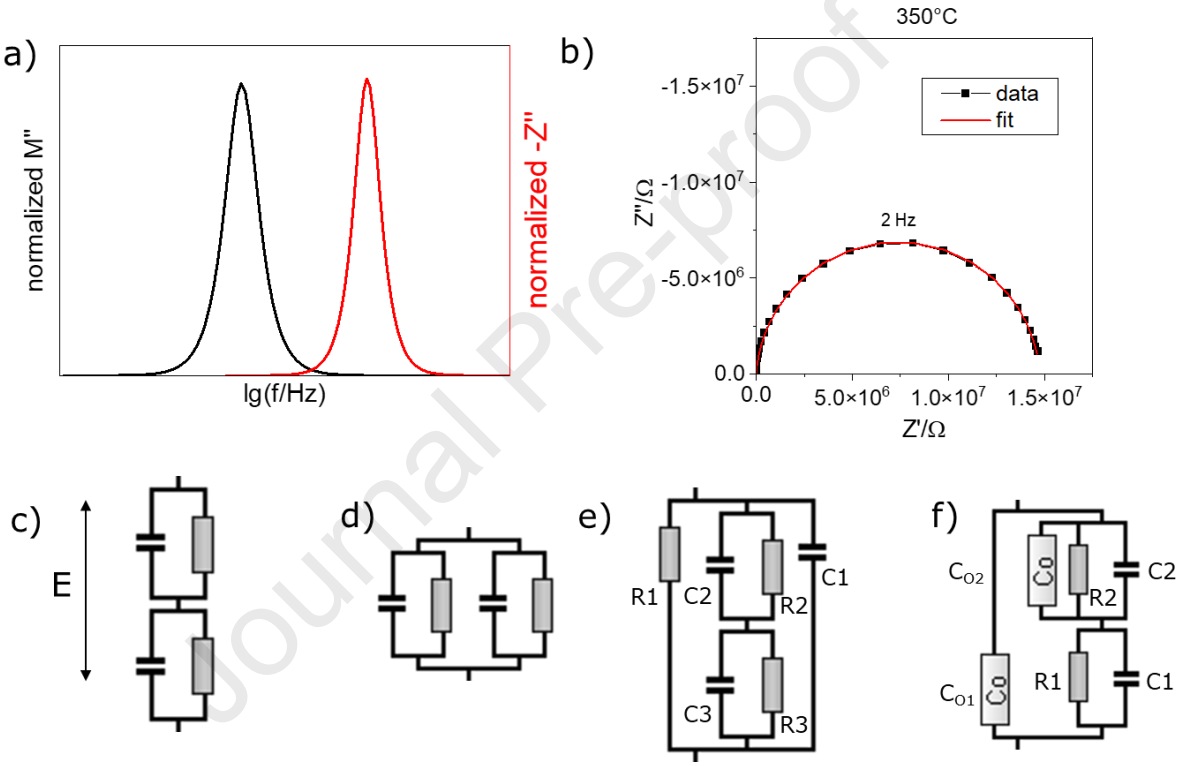

Fig. 3 a) Separation of peak frequencies of imaginary parts of M and Z of a Debye response. b) Impedance spectrum of PZT at 350 °C, which is fitted with one RC circuit. c) Equivalent circuit for two series processes according to the bricklayer theory. E depicts the direction of applied field. d)-f) Equivalent circuits describing possible parallel responses with C_0 as a Debye response.

Another mostly ignored circumstance is that the modulus also highlights parallel contributions to the electrical response [10, 43, 44]. The usually employed bricklayer model (Figure 2 or Figure 3c) treats the grain boundary and bulk responses as homogeneous and connected in series [2, 3]. However, grain size and shape may vary extensively. Furthermore, parallel percolating pathways can occur in the case of chemical and structural heterogeneity. A rather simple example concerning even homogeneous structural and chemical conditions is the measurement of ferroelectric materials [25]. In Figure 3b, the result of an impedance measurement at 350°C of a lead zirconate titanate sample is depicted. A nice semi-circle develops in the Nyquist plot. However, extracting the capacitance from that plot results in a high capacitance for a bulk conductive process ($3.5 \cdot 10^{-8}$ F instead of a value around 10^{-11} F) [10]. The calculated permittivity is approximately 12000. This can be rationalized by taking into account the

high lattice polarizability of the ferroelectric [25]. A temperature of 350°C is close to the Curie temperature, so a high capacitance can be expected. Even at lower temperatures than the Curie temperature, the permittivity does not decrease below 2800. This means that the semicircle in Figure 3b cannot be described only by a conductive process but an additional dielectric process with high capacitance in parallel. As mentioned, even bulk conductive processes exhibit a capacitance due to charge separation [10]. The capacitance of it is, nevertheless, very low. The dielectric process also involves dielectric loss. However, this can also be seen as a minor contribution. Thus, the conductivity/resistance can be rationalized as being in parallel to the lattice polarization. At least in the investigated frequency range, this can be seen as valid. At very low frequencies, the resistance and capacitance from domain orientation can contribute, as well [25]. Therefore, the plot can be fitted only with a RC equivalent circuit instead of a circuit like in Figure 3d with two RC circuits in parallel. Being aware of this relationship, the material can, nevertheless, be investigated and described correctly.

With respect to parallel conducting pathways, a couple of strategies have been employed, e.g., concerning the separation of electronic and ionic transport in mixed ionic-electronic conductors. Equivalent circuits have been developed to quantify the respective contributions [45, 46]. However, in these cases, it has been validated that the spectra contain electronic and ionic contributions beforehand. Therefore, it was known or at least assumed that the evaluation with the used equivalent circuits is valid. Furthermore, the circuits usually contain quite a lot of components, leading to large errors if the parallel contributions cannot be separated. The question remains, whether we can actually identify the presence of a parallel dielectric or conducting pathway from the spectra alone?

In this work, we emphasize the importance of modulus spectroscopy in addition to other standard impedance plots such as Nyquist or Bode plots. Given our motivation to describe the parallel responses in ferroelectric/dielectric material, we elucidate the modulus evaluation of experimental data from lead-free ceramic materials. Furthermore, dielectric simulation results based on physical models, for instance, the electrostatic equation, have direct spatial access to the structure inhomogeneity and defects. The analysis of the simulation data can yield detailed impedance information [47]. Therefore, before applying the modulus analysis on experimental impedance data, we demonstrate the significance of modulus spectroscopy analysis for impedance data based on finite element simulation results involving parallel contributions of grain boundaries and heterogeneities, respectively. Even though the complex electroceramics are used for illustration, the presented evaluation is not limited to electroceramics and can be attributed, e.g., to various composite structures with different electrical responses.

2. Methods

Polycrystalline samples of NBT and $0.8(0.94Na_{1/2}Bi_{1/2}TiO_3 – 0.06BaTiO_3) – 0.2CaZrO_3$ (NBT-6BT-20CZ), a high temperature capacitor ceramic, were prepared by conventional solid-state synthesis. Prior to weighing, the powders (Alfa Aesar GmbH, Germany) Na_2CO_3 (99.5 %), Bi_2O_3 (99.975 %), TiO_2 (99.6 %), $BaCO_3$ (99.8 %), $CaCO_3$ (99.5 %), ZrO_2 (99.5 %), and Al_2O_3 (99.95 %) were dried above 300 °C for 8 h. This allows for obtaining the correct stoichiometry of NBT-based materials[39, 48]. The powders were then ball-milled in a planetary mill (Pulverisette 5 Fritsch, Germany) with zirconia balls and ethanol for 24 h at 250 rpm. Afterward, the slurries were dried at 90 °C for 2 days. The resulting powders were manually ground and calcined at 900 °C (heating rate 5 ^{o}C/min) for 3 h in alumina crucibles. Pellets with a diameter of 10 mm were first uniaxially pressed at 65 MPa, followed by cold isostatic compression (KIP 100E, Weber, Germany) at 380 MPa for 1.5 min. The resulting green bodies were placed in alumina crucibles and covered with sacrificial powder of the corresponding composition to minimize the loss of volatile Bi. Sintering was carried out in air at 1100 °C for 2 h (heating rate 5 ^{o}C/min). The ceramics were then ground, polished, and sputtered with Pt electrodes.

For the synthesis of $K_{0.49}Na_{0.49}Ca_{0.02}Nb_{0.98}Ti_{0.02}O_3$ (KNCN) and $Ca_{0.02}K_{0.48}Na_{0.48}NbO_3$ (CKNN) the following commercial precursors were used: potassium carbonate (99.995%), sodium carbonate (99.999%), niobium(V) oxide (99.99%), calcium carbonate (99.0%) from Sigma-Aldrich. All initial powders were dried at 120 °C for 24h. The stoichiometric amounts of precursors were mixed and milled with 5 mm YSZ (yttria-stabilized zirconia) balls in 250 ml HDPE (high-density polyethylene) bottle with 100% ethanol for 24 h. After milling, the slurry was dried in a rotary evaporator. 25 mm diameter pellets were uniaxially pressed at 5-10 MPa and calcined in a half-closed alumina crucible at the heating rate of 3 °C/min at 825 °C for 4 h with the cooling rate of 10° C/min. Calcined pellets were crushed and milled with 5 mm YSZ balls in 100% ethanol for 24 h. After milling, the slurry was dried in the rotary evaporator and sieved through a 250 µm sieve. Calcined and sieved KNN powder was uniaxially pressed at 100-120 MPa into 10 mm pellets. 0.3 g of powder was used per pellet. Pressed pellets were buried in sacrificial powder and sintered in closed alumina crucible in the air at 1165 °C for 2 h at the heating rate of 5 °C/min and the cooling rate of 10 °C/min.

Impedance spectroscopy was performed with the Novocontrol Alpha-A High-Performance Frequency Analyzer (Novocontrol Technologies, Germany), in the frequency range of 1 Hz to 1 MHz, with an amplitude of 0.1 V from 150 °C up to 650 °C. The subsequent analysis of the resulting impedance data was executed with the help of RelaxIS (rhd instruments, Germany).

Dielectric response of heterogeneous structures is numerically simulated by the finite element method (FEM). In particular, three-dimensional and two-dimensional finite element calculations have been carried out to simulate different electrically inhomogeneous structures with COMSOL (COMSOL

Multiphysics, ver. 5.6, Göttingen, Germany). Two simulation setups were employed. The first 2D setup (26*10*(10) mm^3) emulates the behavior of conductive grain boundaries (Figures 4a and b). The second simulation setup (10*10*4 mm^3) describes the effect of inhomogeneities with electrical properties different than that of the matrix (Figures 4d and c). For the 2D setup, a triangular element is used, while for the 3D setup, the tetrahedral elements are employed. A simulation in the frequency domain was conducted to calculate the linear response to harmonic excitation. For that, the current conservation is calculated based on Ohm's law. The sides of the model are defined as insulating, while the top and bottom are terminal and ground, respectively. Different permittivity and conductivity values are used for the respective phases, and sinusoidal signals were applied to the terminal with an amplitude 1 V. The frequency $f = \frac{\omega}{2\pi}$ ranges from 10^{-3} Hz to 10^{7} Hz and allowed elucidating the effect of electrical heterogeneity on the impedance, modulus, and permittivity spectra. For the grain boundary model in Figures 4 a and b, the grain boundary permittivity $\varepsilon_{\mathrm{gb}}$, the bulk permittivity ε_{b}, the grain boundary conductivity σ_{gb}, the bulk conductivity σ_{b} are taken into account. For the model in Figures 4c and d, different Debye responses in bulk and inhomogeneity/inclusions are simulated to illustrate the impact of varying dielectric responses. The conductivity is set to be the same in all regions ($\sigma_{\mathrm{incl}} = \sigma_{\mathrm{b}} = 1 \cdot 10^{-9}$ S/m). The following equations are used for the real and imaginary part of the permittivity:

$$\varepsilon' = \varepsilon_{\infty} + \frac{(\varepsilon_s - \varepsilon_{\infty})}{(1+\tau^2\omega^2)} \tag{1}$$

$$\varepsilon'' = \frac{\sigma}{\omega\varepsilon_0} + \tau\omega\frac{(\varepsilon_s - \varepsilon_{\infty})}{(1+\tau^2\omega^2)} \tag{2}$$

In which ε_{∞} and ε_s are the high frequency and low frequency limit of the permittivity, respectively. Note that the models represent highly idealized cases. However, conclusions concerning real materials can be obtained from these calculations. In the case of the inhomogeneity model, spherical and elliptical inclusions were chosen to also take into account different voltage drops and field distribution of inhomogeneities. The results were qualitatively, nevertheless, almost identical so that the solution from elliptical inhomogeneities is presented in the following.

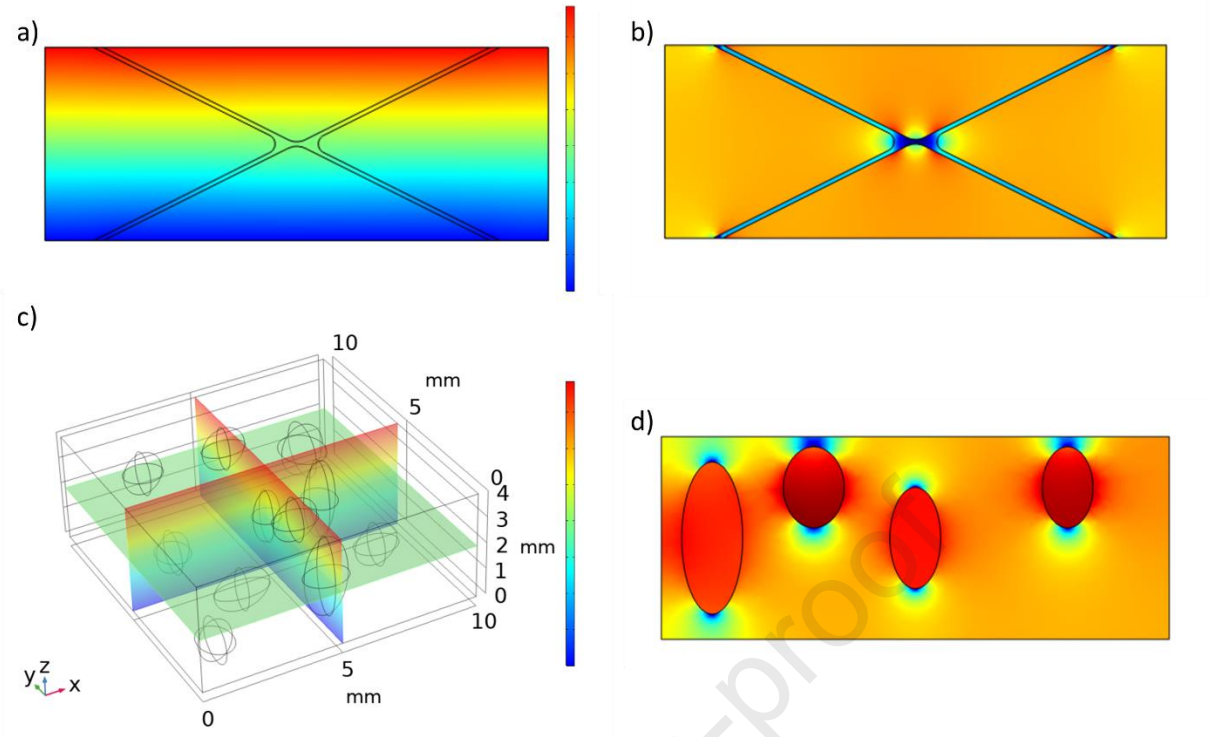

Fig. 4: a) Potential drop from 2D-FEM calculation emulating conductive grain boundaries (color scale from blue to red). b) Electric field E distribution in grain boundary model (100 Hz, $\varepsilon_{gb} = 10$, ε_{b} =100, $\sigma_{gb} = 1 \cdot 10^{-5}$ S/m, $\sigma_{b} = 1 \cdot 10^{-8}$ S/m) c) 3D-FEM model with elliptical inhomogeneities/inclusions (100 Hz, $\varepsilon_{sincl} = 100$, ε_{sb} =75 $\varepsilon_{\infty b} = \varepsilon_{\infty incl}$ =20, $\sigma_{b} = \sigma_{incl} = 1 \cdot 10^{-9}$ S/m, $\tau_{incl} = 1$ s, $\tau_{b} = 1 \cdot 10^{-3}$ s). Color scale from blue to red depicts the potential drop inside the sample. d) yz -Cut slice of FEM model from c at x =5 mm illustrating the average electric field E in the color scale from blue to red.

3. Results and Discussion

3.1. Impedance analysis of electrically heterogeneous structure based on FEM results

FEM calculations of electrically inhomogeneous example structures were conducted to rationalize the resulting impedance results. Figure 4a depicts the potential distribution inside the sample, while Figure 4b describes with average field E inside a sample with parallel conducting pathways like grain boundaries. With the model illustrated in Figure 4c, inhomogeneities having different electrical properties than the surrounding matrix are emulated. These could, e.g., stand for secondary phases, core-shell structures, or PNR distributed in a matrix of different polarity. The respective average field is illustrated in Figure 4d.

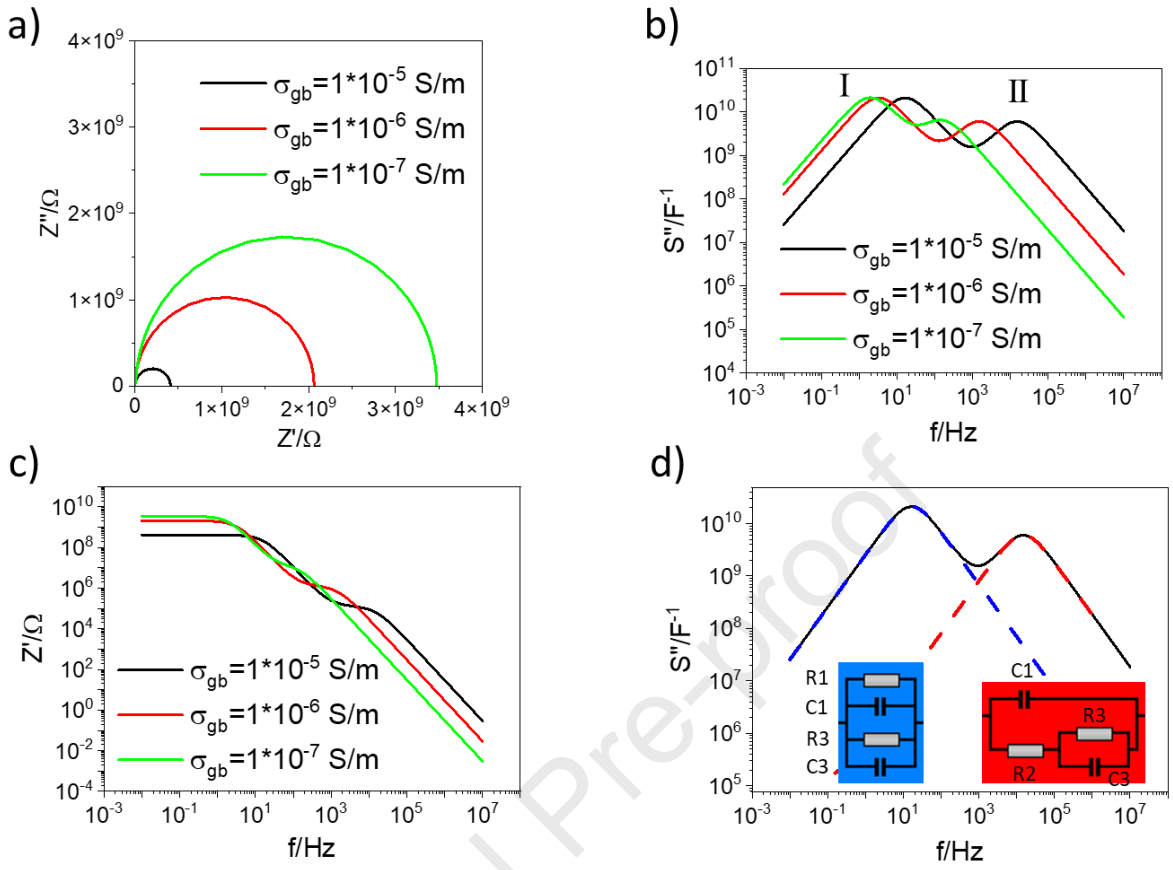

Fig. 5: FEM results for impedance data obtained from the models depicted in Figures 4a and b. a) Nyquist-plot with the model from Figure 4b with varying σ_{gb} ($\sigma_b = 1 \cdot 10^{-8}\, S/m$; $\varepsilon_b = 100$; $\varepsilon_{gb} = 10$). b) Elastance data corresponding to a. c) Z' plotted against frequency. d) Elastance data for $\sigma_{gb} = 1 \cdot 10^{-5}\, S/m$ and fitting with reduced equivalent circuit models illustrating the origin of the two maxima.

3.1.1. Grain boundary pathway model

The plots in Figure 5 depict the FEM results for different grain boundary conductivities σ_{gb} with bulk conductivity σ_b, bulk permittivity ε_b, and grain boundary permittivity ε_{gb} kept constant. In Figure 5a, a decrease in resistance can be observed with increasing grain boundary conductivity. However, there is no secondary process evolving in the Nyquist-plot. Only in the Bode-plot, where the Z' is plotted against frequency, a second resistive response is visible (Figure 5c). This means that the pathway also contributes with a frequency dependent serially connected response. Figure 4a does not represent an ideal parallel pathway. However, the higher the conductivity of the grain boundary becomes, the lower the series electrical contribution. The respective high frequency plateau in Figure 5c could be mistaken as a high bulk conductivity of the polycrystalline structure if the components' physical properties are not known *a priori*. In Figure 5b, the imaginary part of the elastance S'' is plotted against the frequency. The complex elastance S^* is essentially the modulus but not taking into account the sample/component dimensions:

$$S^* = \frac{M^*}{C_0} = \frac{M^* \cdot d}{\varepsilon_0 \cdot A} \tag{5}$$

It is important to use the elastance instead of the modulus, as we cannot judge the electrical impact and geometry factors of the different components at this point. Interestingly, a second high-frequency process (described with II) is visible in the elastance plot in Figure 5b. Similar to the shoulder response in Figure 1b, it has a lower elastance value than the low-frequency response I. For this model, this cannot be explained by electrical responses connected in series. Instead, it is a clear sign of parallel electrical pathways set up by the models in Figure 4. From the evaluation of Figure 5b, it becomes apparent that the separation of the two peaks, and hence the opportunity to distinguish the two processes, increases with large differences in σ_{b} and σ_{gb}. Furthermore, it is beneficial if the permittivities of bulk and grain boundary show moderate differences for this behavior to occur, as well. This is illustrated in the ESI in Figure S1 for a constant conductivity difference. In case ε_{b} is one order of magnitude larger than $\varepsilon_{\mathrm{gb}}$, the high-frequency response II in Figure S1b is smaller than the low-frequency response I. For equal permittivity, hardly any second peak develops, and for permittivity being two orders of magnitude higher, there is a reversal in peak height. This means that in this case, the response does not look any different from a series response that the bricklayer model usually evaluates (Figure 2e). That would mean that the parallel and series models are again indistinguishable, and knowledge about the physics would need to be gathered in a different way before attributing an equivalent circuit model to the impedance response. The real part of the capacitance in Figure S2 in the ESI illustrates that there is a transition from the low permittivity contribution of ε_{gb} to ε_{b} at varying frequencies with changing σ_{gb}. These frequencies coincide with the respective peaks in the elastance in Figure 5b. This means that the elastance peak is still linked with a transition in capacitance but does not allow for simple quantification of capacitance as in the case of a bricklayer model, in which all responses are connected in series (Figure 1e). Due to the contributions of the processes being parallel and in series, the frequency peaks in the elastance plot depend on the permittivity/capacitance of both processes, which are not easily separated. The best equivalent circuit model to describe this behavior is given in Figure 3e. In this case, we can express the elastance by the admittance contributions Y:

$$S^* = \frac{j\omega}{Y' - jY''} \tag{6}$$

$$S^* = \frac{j\omega}{\frac{1}{R_1} + j\omega C_1 + \frac{1}{Zs}} \tag{7}$$

Where R_1 and C_1 are the respective components in Figure 3e, and Zs is the impedance of the third pathway with two RC responses in series. Therefore the elastance can also be expressed as:

$$S^* = \frac{j\omega}{\frac{1}{R_1} + j\omega C_1 + \frac{1}{\frac{R_2 - j\omega C_2 R_2^2}{1+(\omega C_2 R_2)^2} + \frac{R_3 - j\omega C_3 R_3^2}{1+(\omega C_3 R_3)^2}}} \tag{8}$$

At this point, the conductivity and permittivity of bulk and grain boundary cannot be directly obtained without fitting. However, depending on certain approximations, the respective contributions can be partly quantified. To achieve this, the origin of the two maxima in the imaginary elastance plot (Fig. 5b) needs to be elucidated. The initial conditions are that C_1 has the largest capacitance value and that $R_3 > R_2$ and $C_3 > C_2$. For low frequencies, the contribution of R_2 and C_2 become negligible, and the behavior can be approximated by the equivalent circuit shaded in blue in Figure 5d. The frequency at which the maximum occurs in S'' becomes:

$$\omega_{max\,I} = (R_1 + R_3)/(R_1R_3C_1 + R_1R_3C_3) \tag{9}$$

and

$$S''_I = (R_1^2R_3 + R_3^2R_1)/(\,2(R_1 + R_3) \cdot (R_1R_3C_1 + R_1R_3C_3)). \tag{10}$$

Only in the case of $C_1 \gg C_3$ and $R_1 \gg R_3$ we can approximate further so that we obtain $\omega_{maxI} = 1/(R_3C_1)$ and $S''_I = 1/2C_1$. For the case in Figure 5, it can at least be determined that the capacitance of low frequency peak in Figures 5b and d, which is essentially the frequency independent C_1, is close to the capacitance if no grain boundary phase was present. Thus, the bulk permittivity ε_b can be derived in this case.

At higher frequencies, R_1 starts to play less of a role and instead R_2 contributes to the electric response (equivalent circuit in Figure 5d shaded in red). Even R_3 may become less relevant. Thus, for peak II in Figures 5b and d:

$$\omega_{maxII} = (C_1 + C_3)/(C_1R_2C_3) \tag{11}$$

and

$$S''_{II} = C_3/\big(2C_1(C_1 + C_3)\big). \tag{12}$$

Again, for $C_1 \gg C_3$ $\omega_{maxII} = 1/(R_2C_3)$. This means that ω_{maxII} becomes independent of C_1. The imaginary elastance value, however, still depends on the two capacitance contributions. Therefore, it is possible to obtain the major parallel capacitance C_3 with C_1 and Eq. 12. R_3 and R_2 can be obtained from the approximate descriptions of ω_{maxI} and ω_{maxII}, respectively. To further calculate R_1 , only the first approximation of ω_{maxI} in Eq. 9 can be used. C_2 as the capacitance of the highly conductive process is too low to be quantified in this case. As mentioned before, ε_b can be calculated from C1. The actual conductivity of the grain boundary and the bulk can, however, not be obtained. The real axis intercept in Figure 5c and thus the dc resistance equals R_3. Therefore, a large error is expected for the calculation of R_1 as it hardly contributes to the spectrum (just like C_2). R_3 and R_2 can be attributed to the bulk and the grain boundary, respectively. However, because of the complex current

pathways the calculation of the corresponding conductivities is not possible. Nevertheless, the involved mechanisms can still be rationalized with, e.g., Arrhenius plots from temperature dependent, because the activation energies of the processes do not depend on the sample dimensions. With equivalent circuit fitting using the model in Figure 2e, it is, of course, possible to obtain all contributions, but the error can be quite large in this case. Thus, quantifying the resistances can be challenging. The evaluation of Fig. 5d shows that a reduction of complexity of the respective equivalent circuit is possible in many cases. However, we propose that either this or the following model are as likely as the simple bricklayer model in inhomogeneous electroactive materials. Thus, these should be taken as a starting point when parallel pathways start to significantly contribute to the overall response.

The spectra in Fig. 5c could also be attributed to the physically wrong bricklayer model in Fig. 2d. In this case, false conclusions could be drawn, like high bulk conductivity and low grain boundary conductivity. Therefore, the modulus representation can provide the opportunity to identify the correct physical mechanism leading to the frequency dependent electrical response.

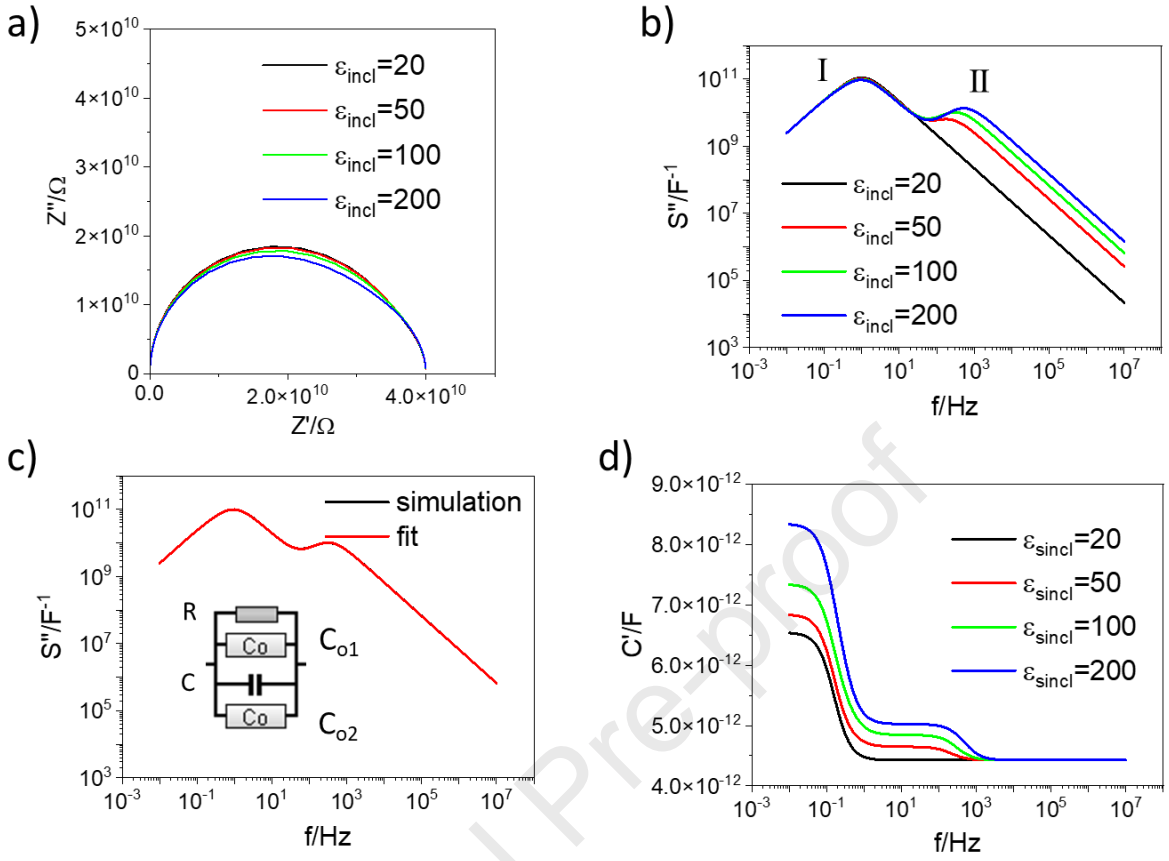

Fig. 6: FEM results for impedance data obtained from the models depicted in Figures 4c and d (ε_{sb} =30, $\varepsilon_{\infty b} = \varepsilon_{\infty incl}$ =20, $\sigma_b = \sigma_{incl} = 1 \cdot 10^{-9}$ S/m, $\tau_b = 1$ s, $\tau_{incl} = 1 \cdot 10^{-3}$ s). a) Nyquist-plot with the model from Figure 4c and d with varying ε_{sincl}. b) Elastance data corresponding to a. c) Elastance data from ε_{sincl} =100 with fit from equivalent circuit depicted in the inset. d) C' plotted against frequency.

3.1.2. High permittivity inclusion model

Modeling PNR or the contribution of ferroelectric polarization to the permittivity just by a medium with a defined resistance and high capacitance should not be appropriate. These are rather dielectric processes and do not resemble long-range charge transport. Therefore, we introduced a Debye response in parallel to a long-range conductive response for every phase in Figures 4c and d to model a dielectric behavior. The plots for different low-frequency permittivity limits of the inhomogeneity or inclusion Debye process values ε_{incl} are given in Figures 6a to d. The low-frequency permittivity limit of the bulk is always set at ε_{sb}= 30. The conductivity of the phases (σ_b for the bulk and σ_{incl} for the inhomogeneity) is the same. The high-frequency limits of the two Debye responses ($\varepsilon_{\infty b}$ and $\varepsilon_{\infty incl}$) are equal as well. There is, however, a significant difference in the relaxation time τ introduced between bulk and inhomogeneity ($\tau_{incl} = 10^{-3}$ s and $\tau_b = 1\ s$). Therefore, any detected differences in the model depend on the low-frequency permittivity limits of the Debye responses. The Nyquist-plot in Figure 6a shows hardly any differences with respect to changes in ε_{sincl}. However, there may occur a very small bulging of the semicircle at low frequency for high ε_{sincl} compared to the low-

frequency permittivity of the bulk ε_{sb}. Such a response also regularly develops for electrode processes in series to the bulk response [40] and could be confused with the present response. In Figure 6b, the progression of S'' with increasing ε_{incl} is depicted. The high frequency elastance peak II increases with higher ε_{sincl}. This means that a lower response at high frequencies may indeed be the result of a highly polarizable phase inside of a matrix with lower permittivity. However, there is no increase in long-range conductivity. It is merely the difference in permittivity and τ leading to the observed responses. Therefore, the second resistive response in Figure 6c does not reflect a highly conductive phase. Nevertheless, the overall bulk conductivity σ_b can be obtained from the low-frequency plateau for this model. Concerning the quantification of the influence of the different Debye-responses on the capacitance, it actually makes more sense to directly evaluate the real part of the capacitance C' plotted against frequency (Figure 6d). The plateau from 10^{-5}-10^{-7} Hz is dominated by the response of $\varepsilon_{\infty\mathrm{b}} = \varepsilon_{\infty\mathrm{incl}}$ =20. The respective value can directly be calculated from the capacitance in that region. Coming from higher frequencies to lower ones, there is first the transition to ε_{sincl} at 1 kHz because we set $\tau_{incl} = 10^{-3}$ s. Even though the volume fraction of the inhomogeneities is 35% and there is a 10 fold increase in ε_{sincl} for the blue line in Figure 6d, the increase in capacitance is not very extensive (by a factor of 1.2). This means that the bulk permittivity still dominates the electrical response. It is hardly possible to derive the value of ε_{sincl} from the capacitance unless the dimensions of the inclusions are known. At 1 Hz ($\tau_b = 1\ s$) there is a further rise in capacitance due to the transition to $\varepsilon_{\mathrm{sb}}$ =30. For this model, it becomes clear that the identification of parallel pathways can be made using the modulus representation. The quantification of the capacitance values for the contributing processes is, nevertheless, best done from the plateaus in the plot of C' against frequency (Figure 6d). Even though the equivalent circuits given in Fig. 3 can be seen as the complex general models, a reduction in complexity can be achieved for the present model, similar to the discussion of the previous grain boundary model in Figure 5d. An appropriate equivalent circuit to fit the data in Fig. 6 is a reduced one from the circuit in Figure 3 f) as the conductivity in the two regimes and the ε_{sb}= 30 remain the same. The elastance data, the fit, and the equivalent circuit are depicted in Fig. 6c. Co stands for Cole-Cole-element in this case given by the Relaxis software:

$$Co = \frac{C_C}{1+(i\omega\tau)^{\alpha}} \tag{12}$$

where C_C represents the capacitance. If $\alpha = 1$ then Eq. 12 becomes a simple Debye relaxation which the fit parameters expectedly illustrated for the two processes. Essentially, this approach is similar to the description of the general ferroelectric in Fig. 3b. However, there are two different dielectric responses in parallel because of the presence of, e.g., polar nano regions with significantly different dielectric properties. The values for $\tau_{incl} = 10^{-3}$ s, $\tau_b = 1\ s$ and the conductivity can also be rationalized. With the value of the regular capacitance C_1, the value for C_{C1} for which $\tau_b = 1\ s$ and the dimensions of the model in Figure 4c ε_{sb}, $\varepsilon_{\infty\mathrm{b}} = \varepsilon_{\infty\mathrm{incl}}$ can be calculated, respectively. In principle,

C_{C2} represents the response from the inhomogeneities but quantification of ε_{sincl} remains challenging. As mentioned, the geometric factor for the calculation is unknown or at least very complex. Nevertheless, assuming a rectangular shape of the inhomogeneities and averaging the size variations, it is possible to obtain ε_{sincl} values with about 20% deviation from the actually used values. In the ESI in Figure S3 the results of a similar calculation are given. In this case, however, $\tau_{incl} = 1$ s and $\tau_b = 10^{-3}\ s$, which mean that the values are reversed and τ_b affects the spectra first when coming from high frequencies. The ε_{sincl} =100, and instead, the ε_{sb} is varied. There is basically no influence on the Nyquist plot at all for this model (Figure S3a). The elastance in Figure S3b illustrates that there needs to be a reasonable difference in ε_{sincl} and ε_b. Otherwise, the high-frequency peak II is higher than peak I, which makes a parallel pathway again indistinguishable from a bricklayer model, at least in the elastance plot (Figure 2e). The capacitance is again best quantified by investigating the C' plotted against frequency directly instead of using the S'' peak values. In this case, it can also be seen that there is a larger change in capacitance at higher frequencies. This again is not in line with a bricklayer model. Hence, evidence on the presence of a parallel pathway is obtained by comparing modulus and permittivity.

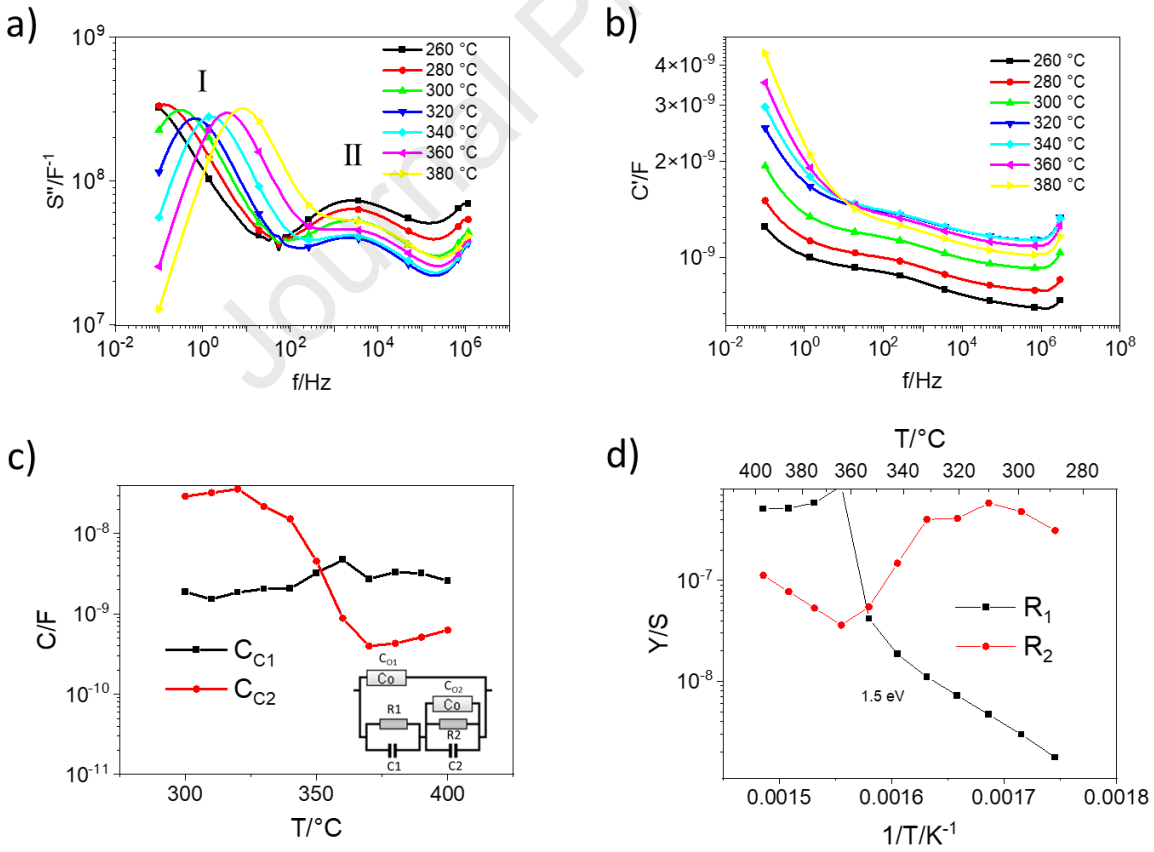

Fig. 7: a) S'' plotted against frequency for pure NBT at varying temperatures. b) Frequency dependent C'corresponding to data from a. (Symbols every ten data points for illustration) c) Values for the capacitances of Cole-Cole elements from fits of NBT data with the equivalent circuit from Figure 3f (again illustrated in the inset). d) Arrhenius plot for the admittances from fits of NBT data with the equivalent circuit from Figure 3f.

3.2. Evaluation of modulus data from electroceramics

3.2.1. NBT-based piezoceramics with regions of different permittivity

In the following, some ceramic materials are discussed to show how common such a heterogeneous response is. In Figure 7a, the modulus data from the measurement of pure NBT is given for various temperatures. Similar spectra could also be observed in previously investigated NBT-based compositions [49] in which the M'' or S'' peaks have already been attributed to PNR responses. A clear separation of the peaks is visible, but only one semi-circle can be obtained from a Nyquist-plot (see Figure S4a in the ESI). Furthermore, a second response is hardly visible in Figure S4b, in which the Z' is plotted against frequency. Therefore, the only clear hint towards a possible parallel electrical pathway is peak II in the plot of S'' against frequency. A fit according to the bricklayer model would certainly result in deviations at high frequencies in Figure S4b, but these would not be very extensive and could be circumvented by narrowing the fitted frequency range. With increasing temperature, the low-frequency peak I in Figure 7a first decreases and then increases again at 360°C, while also shifting to higher frequencies. The frequency shift can be attributed to the increase in overall conductivity with temperature [50]. In Figure 7b, C' is plotted against frequency. Similar to the model described in Figure 6d, two plateaus are visible at high frequencies with a further low-frequency rise in capacitance. This could be attributed to the general polar response of the lattice at high frequency and dielectric Debye response with a τ around 10^{-4} s. There does not seem to be a shift in τ, which is in good agreement with the stable peak II position in S'' in Figure 7a.

It is possible to nicely fit the spectra from Figure 7 with the equivalent circuit in Figure 3f. A reduction of the complexity of the equivalent circuit, like it was done for the model investigation with parallel dielectric responses (section 3.1.2), was not possible in the present case. Most interesting are the capacitances C_1 and C_2 (representing essentially ε_∞ in Eqs. 1 and 2 for the two dielectric responses) and the capacitances C_{C1} and C_{C2} (representing ε_s of the two phases, respectively). In Figure 7c, it can be seen that there is a transition from dominant C_{C2} to a dominant C_{C1} at 350°C. The same is valid for C_1 and C_2 (Figure S5). This is well in line with the structural and permittivity changes at this temperature. The phase coexistence regime between rhombohedral and tetragonal structures ranges from about 200°C to 400°C [35]. These structures are attributed to the two types of PNRs. Therefore, the change in capacitances illustrates the transition from low temperature to high temperature PNRs with 350°C as temperature at which both types contribute the same to permittivity. This is essentially also the maximum of the overall permittivity response. Hence, the results can be seen as further proof for the present interpretation of the underlying physics in NBT. Furthermore, it is now possible to identify more about the dielectric properties of each PNR type. The C_{O1} can be attributed to the tetragonal PNRs because of its dominance at high temperature [35]. C_{O2} should be the response of the low temperature rhombohedral PNRs. Their time constants (τ_1 and τ_2, respectively) vary with

temperature, as well. However, τ_1 is always higher that τ_2. While τ_1 ranges from 140 Hz to 0.14 Hz, the τ_2 values are between 0.0088 and $8*10^{-5}$ Hz. This rationalizes the significant frequency dependence of temperature dependent permittivity. Not only does the capacitance change with temperature, but the contribution of the different PNRs highly depends on the frequency because of the different time constants. Additionally, it can be said that the rhombohedral PNRs are easier to polarize or more polarizable than the tetragonal PNRs. The temperature dependent admittances obtained from resistances (R_1 and R_2) of the fits do not seem to make sense physically at first glance. In Figure 7d, the admittance is given for the two processes in an Arrhenius plot. Focussing first on the low temperature regime, the admittance of the first process Y_1 is very low and it has an activation energy of 1.5 eV. This generally speaks for intrinsic electronic conductivity [48]. The admittance for the second process Y_2 is much higher in the low temperature regime, but there is a complete reversal of the Y_1 and Y_2 values at 350°C, which was previously identified as the actual transition temperature between the two types of PNRs. This nicely shows again that there is a switch in the dominance of the mechanisms. The PNRs with the rhombohedral phase become the “inhomogeneity”, while tetragonal PNRs become the “matrix”. One resistance response can, therefore, be attributed to the overall bulk resistance and the other rather to the loss parallel to the inhomogeneity capacitance. Compared to the high permittivity inclusion model, it becomes clear that most electrical data could have been derived by evaluating the spectra in the present case, as well. However, especially concerning the temperature dependent changes, fitting helped to understand the underlying processes better. Furthermore, the measurement results are more complex than the model as more parameters need to be taken into account.

The effect from PNRs should disappear at the so-called Burns-temperature. At this temperature, the influence of PNR does not impact the permittivity anymore. However, various values are given in literature, with the latest work illustrating a PNR impact to still be present at 700°C for NBT based material [51]. This is beyond the highest temperature used in this experiment. However, the Burns-temperature usually decreases in solid solutions with BT and CZ.

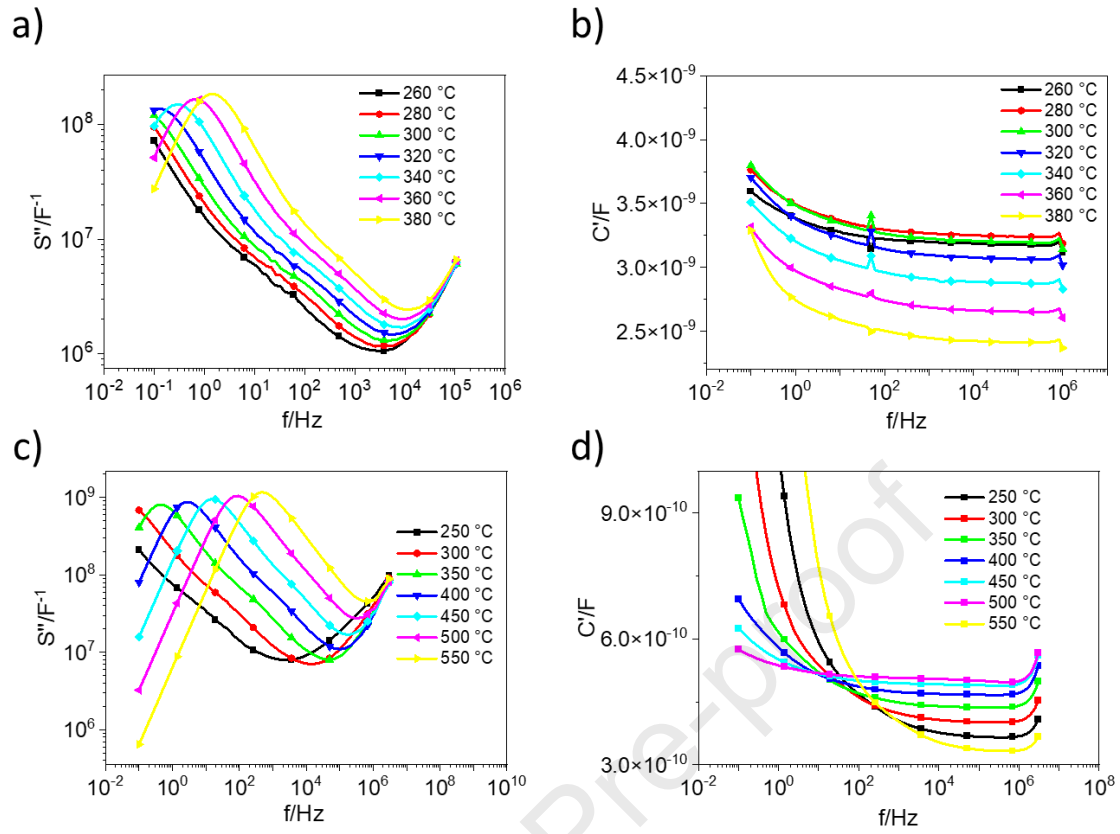

Fig. 8: a) S'' plotted against frequency for NBT-BT at varying temperatures. b) Frequency dependent C'corresponding to data from a. c) S'' plotted against frequency for NBT-BT-20CZ. d) Frequency dependent C′ of NBT-BT-20CZ (Symbols every ten data points for illustration)

The results of a measurement of an NBT-BT material with 6% BT content are given in Figures 8a and b. This material is far more often discussed in literature because of its excellent ferroelectric properties [27]. Pure NBT is not of interest for ferroelectric applications. For the BT containing composition temperature dependent measurements have been conducted, as well. The separation of the S'' peaks is not as clear as for the pure NBT (Figure 7a) or other published data on NBT-based material [34, 37, 49]. However, it can be assumed that similar mechanisms as for NBT are responsible for the observed behavior. Nevertheless, fitting with an equivalent circuit leads to large errors because the high frequency response in Fig. 8a can only be observed as a small shoulder. Thus, only a qualitative evaluation of the data is possible at this point. The real part of the capacitance C' is given in Figure 8b, and there is only one plateau visible. Comparing this to the model case in Figure 6d, this could mean that the contribution of the respective second dielectric response is smaller compared to NBT. However, also in this case, this would mean a highly polarizable phase is present but with a lower concentration or lower permittivity. Thus, this backs up earlier reports [10, 25, 34, 37]. However, a variation in conductivity, as often hypothesized, is not present, and the response can rather be solely attributed to variations in permittivity. The low-frequency S'' shoulders for temperatures up to 300°C cannot be resolved due to the limited frequency range (Figure 8a). Nevertheless, the capacitance

shows a maximum plateau for 280°C (Figure 7d), which again correlates with the broad peak maximum for the permittivity of NBT-BT. Note that the increase in permittivity and modulus at the highest frequencies of the data in Figures 8a and c is an artifact resulting from the measurement setup. When it comes to the high-temperature capacitor material NBT-BT-20CZ described in Figures 8c and d, temperature dependent results also show similar behavior to NBT-BT. In this case, the Burns-temperature should be significantly lower than for NBT and NBT-BT (around 420°C), and it can be seen in Figure 8c that at 450°C, the S'' shoulder II is practically invisible. The result further backs up the interpretation of PNR being responsible for the high-frequency modulus response. This, however, is not what was found for every material investigated in previous publications [34, 37]. For some samples, the peak actually did not disappear far above the Burns temperature. A possible explanation for this is the formation of a core-shell material, which could be determined in similar cases [39, 52]. NBT materials are prone to develop a core-shell structure under certain conditions [29, 30, 53, 54]. Therefore, the two peaks could still be present above the Burns temperature and represent the interaction between core and shell properties. This will, however, be further elucidated in future publications.

3.2.2. KNN-based ceramics with regions of different conductivity

The NBT-based ceramics are structurally and chemically quite complex. Nevertheless, it is fascinating to see how much information on the physical properties can be obtained just by conducting frequency dependent electrical measurements. A lead-free ferroelectric material that does not easily develop relaxor behavior but can be chemically heterogeneous is $K_{0.5}Na_{0.5}NbO_3$ (KNN) and its solid solutions [55]. Variations in chemical compositions can even be caused in pure KNN by using different types of Nb educts. This leads to changes in the calcination and sintering properties and eventually results in a core-shell structure. In the present case, different Ca-doped samples were chosen. Due to the ionic radius of Ca, it should, in principle, be possible for Ca to enter the A- and the B-site. Therefore, two compositions with 2% Ca-doping were synthesized.

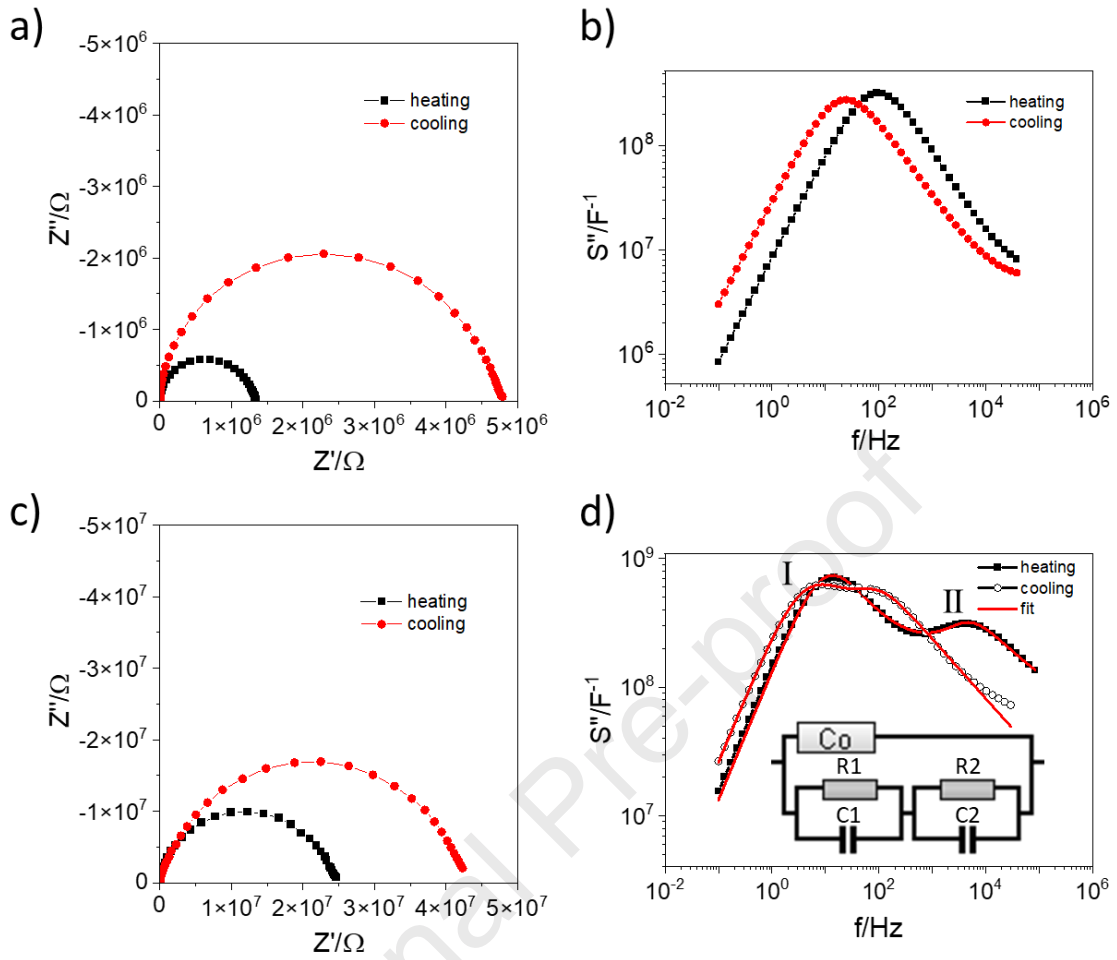

Fig. 9: a) Nyquist-plot for CKNN measurement at 400°C during heating and cooling step. b) S'' plotted against frequency corresponding to Nyquist plot in a. c) Nyquist-plot for KNCN measurement at 400°C during heating and cooling step. d) S'' plotted against frequency corresponding to Nyquist plot in c. Fits with model from Figure 3e are given in red.

The grain size and morphology change, but no sign of chemical heterogeneity can be observed from the SEM data (Figure S8 in the ESI). However, for both materials, a common but small Nb-rich secondary phase can be determined in the XRD-data (between 25° and 30° in Figure S9 in the ESI). The impedance data were recorded during heating up to 600 °C and during cooling down to room temperature. This revealed a change in resistance at around 600 °C for both samples. In Figures 9a and c, the Nyquist-plots of data from CKNN (A-site doping) and KNCN (supposed B-site doping) obtained at 400°C in the heating, and cooling steps are given. The resistance increases about a factor of 2 to 3 after heating, which is an irreversible process. This hints toward metastable defect chemistry, which could have resulted from a comparably fast cooling after sintering. The defect chemistry of a high temperature state could have been frozen in. If only the Nyquist plots are compared, the samples behave very similarly. However, the impedance of KNCN in Figure 9c is about an order of magnitude higher. Nevertheless, if the assumption of A-site or B-site occupation is true, the difference might be larger as we would expect a donor and an acceptor doped sample, respectively.

Also in this case, the differences in the samples actually become better elucidated by evaluating the elastance. The plots in Figures 9b and d are very different. For the CKNN, there is only one peak in S'', hinting toward a homogeneous electrical response (Figure 9b). The cooling step's peak has a lower value and is shifted to lower frequencies compared to the heating step. This expresses the same behavior as can be derived from the Nyquist plot in Figure 9a, an increase in capacitance and resistance. In Figure 9d, two peaks are visible where the low-frequency S'' peak I has a higher modulus value than peak II. The low-frequency peak I shifts slightly compared to the peak of the CKNN material in Figure 9b. However, the high-frequency peak changes drastically and starts converging with the low-frequency peak after heating.

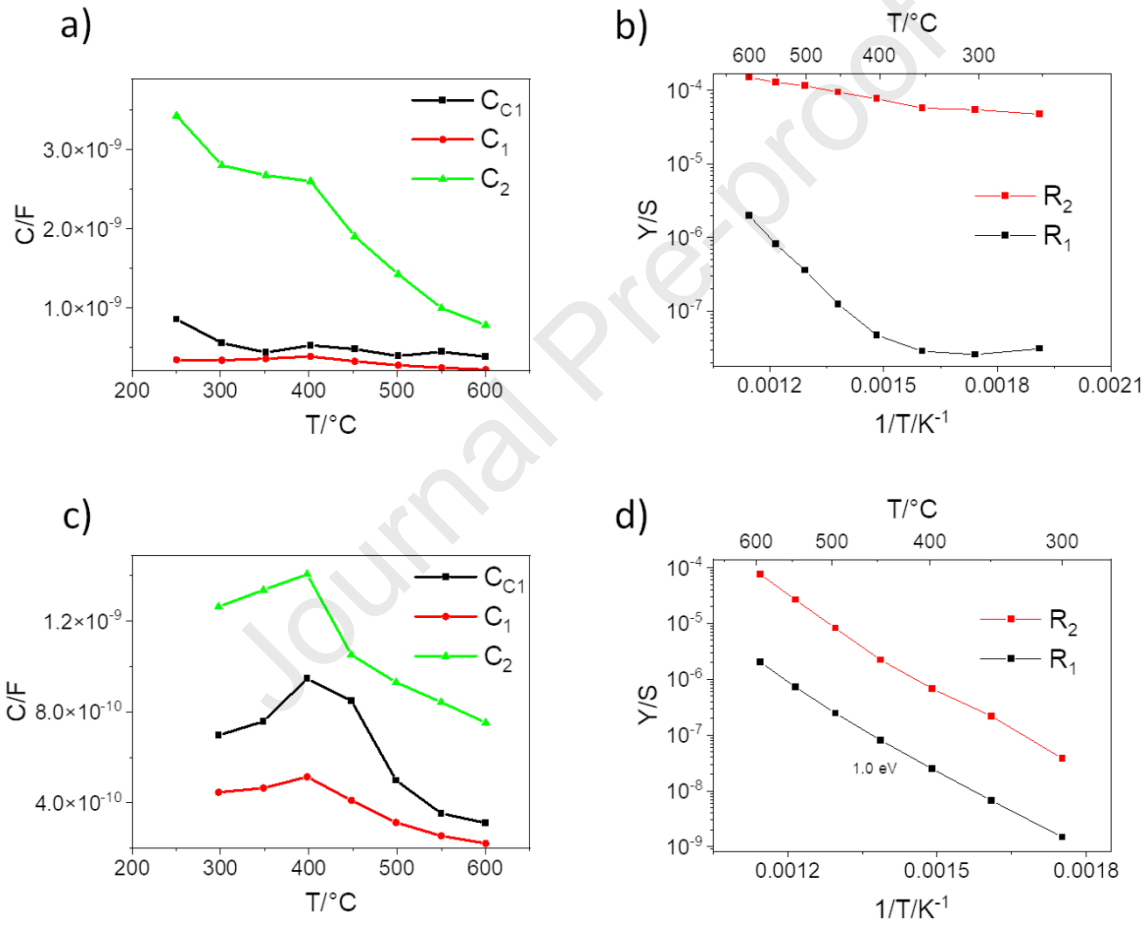

Fig. 10: Fit parameters from equivalent circuit depicted in Fig. 9d of impedance spectra of KNCN during heating step: a) Capacitance values, b) Resistance values. Fit of KNCN during cooling step: c) Capacitance values, b) Resistance values.

As large changes in conductivity are observed, it was first assumed that the spectra von KNCN can be fitted with the equivalent circuit model in Fig. 3e, which would mean a fast parallel charge transport. However, this did not work out. Instead, a modified circuit from Fig. 3f needs to be used. This is illustrated in the inset of Fig. 9d. Thus, there is actually a dielectric process in parallel to two resistive processes in series. The fit data from the heating step of KNCN are shown in Fig. 10a and b. In Fig. 10a, it seems as if the capacitances C_{C1} and C_1 stay almost constant with temperature while C_2 decreases.

The resistances in Fig. 10b are significantly different, and the higher resistance R_1 seems to exhibit an extrinsic electronic contribution at low temperatures. However, keeping the material at 600°C with multiple measurements at that temperature revealed that the processes kept changing drastically. This change most likely started at lower temperatures already. Therefore, it is not possible to derive reasonable physical properties from the heating step data. The cooling step results are given in Fig. 10c and d. For the capacitances in Fig. 10c, there is always a peak visible around 400°C. This reflects the expected phase transition [56]. However, as investigations were only conducted at few temperatures, this phase transition cannot be resolved as nicely as with permittivity measurements in a limited frequency range. Nevertheless, it leads to the conclusion that the capacitances can all be attributed to the dielectric lattice polarization where C_{C1} contributes to ε_s, and C_1 and C_2 to ε_∞ values being parallel to two different resistances. The values for the respective admittances are shown in Fig. 10d. There is still a difference in the magnitude of the resistance, but the activation energy of the processes is exactly the same. As mentioned, this can be the case for bulk and grain boundary resistances. If we attribute R_2 and C_2 to the grain boundary, we get a high capacitance but a lower impact on the total resistance. We, nevertheless, need to keep in mind that the local resistivity of the grain boundaries is most likely much higher because they are much thinner than the bulk. If this is the case, it becomes clear that the grain boundary process changes much more significantly than the bulk process during heating. The capacitance and resistance of the grain boundary are drastically different comparing the heating and the cooling step. Thus, it can be assumed that the thermal annealing led to an equilibration of the defect chemistry at the grain boundary to a thermodynamically more stable condition.

As a result, the CKNN sample changes its properties homogeneously during temperature treatment. KNCN is heterogeneous, and the electrical response could be explained by a grain boundary or grain boundary-near phase changing its properties with temperature. Most likely, the assumption that calcium can fit onto the B-site is not valid, and we obtain a heterogeneous ceramic. However, no hint of significant secondary phase development or core-shell structure could be found, as indicated by the XRD results. Therefore, further investigations are necessary to fully elucidate the origin of the second response. Nevertheless, the evaluation of the KNN samples serves as a further good example for complex heterogeneous electrical responses that demand an evaluation with parallel electrical contributions beyond the bricklayer model.

3.3. Steps during evaluation of inhomogeneous electroactive materials

Irrespective of what type of material is the focus of an investigation, it is possible to narrow down the necessary steps to rationalize the underlying physical mechanisms.

a) Firstly, the representation of primary interest should be determined. This is usually the capacitance, impedance, or admittance for dielectric/ferroelectrics, resistors, and conductors, respectively.
b) The identification of a possible parallel electrical process can be made using the modulus representation like described above.
c) Elucidating whether the parallel response is a dielectric or a conductive one is important, as well. It is possible to derive information about this from temperature dependent measurements as depicted in Fig. 7c for the NBT. The first peak changes with temperature and is affected by conductivity, while the second peak results from interactions of capacitive responses. Furthermore, the relationship between the peak maxima in Z'' and M'' can be used as illustrated in Fig. 3a [42].
d) After identifying the respective mechanisms, a physical model based on the ones described in sections 3.1.1. and 3.1.2. can be attributed to the spectra. Often, it can be useful to obtain respective values for the corresponding contributions from the spectra directly. However, using an equivalent model fit can help rationalize whether the approximations to reduce the problem in sections 3.1.1. and 3.1.2. are actually valid. As can be seen in, e.g., section 3.2.1, the physics were more complex for the experimental data of NBT, and thus the full equivalent circuit model in Figure 3f was necessary for the fit instead of the reduced one in Fig. 6c.
e) Finally, it needs to be rationalized whether the sample dimension independent values like conductivity, resistivity, and permittivity can be quantified for the involved processes. The complex conditions in inhomogeneous samples may not allow that.

4. Conclusions

The presented examples of impedance data from electroceramics illustrate the power of evaluating all types of representation of the same frequency dependent electrical data. Especially the modulus or elastance representation gives rise to possible parallel responses (dielectric or conductive). In the case two responses are visible when the imaginary part of the elastance S'' is plotted against frequency and the high frequency peak obtains the smaller S'' value, the material can hardly be described with an equivalent circuit model with only electrical responses in series. Thus, evaluating the elastance/modulus allows for discerning series responses and parallel electrical responses. Based on the evaluation of spectra from lead-free electroceramics, it could be shown that parallel electrical responses occur quite regularly in structural or chemically heterogeneous materials. Even though the

work focuses on dielectric and ferroelectric ceramics, the approach and findings can be attributed to many other cases of impedance measurements. In this way, parallel dielectric or charge transport processes in heterogeneous compounds like composites can be elucidated and even quantified.

Conflicts of interest

There are no conflicts to declare.

Acknowledgements

Maximilian Gehringer, An-Phuc Hoang, and Till Frömling gratefully acknowledge the German Ministry of Education and Research (BMBF) for funding of the Young Investigator Group HTL-NBT within the program "NanoMatFutur" [Grant No. 03XP0146]. Sebastian Steiner and Till Frömling are thankful for the financial support by the Deutsche Forschungsgemeinschaft (DFG) through project Grant No. FR 3718/1-1. Bai-Xiang Xu would like to thank the DFG (Grant No. Xu 121/6-1) for the funding.

References

[1] A.-K. Huber, M. Falk, M. Rohnke, B. Luerßen, L. Gregoratti, M. Amati, J. Janek, Physical Chemistry Chemical Physics 14 (2012) 751-758.
[2] J. Fleig, Solid State Ionics 131 (2000) 117-127.
[3] J. Fleig, J. Maier, Journal of the European Ceramic Society 19 (1999) 693-696.
[4] S.I.R. Costa, M. Li, J.R. Frade, D.C. Sinclair, RSC Advances 3 (2013) 7030-7036.
[5] W. Preis, A. Bürgermeister, W. Sitte, P. Supancic, Solid State Ionics 173 (2004) 69-75.
[6] B.A. Boukamp, Solid State Ionics 169 (2004) 65-73.
[7] K. Funke, R.D. Banhatti, S. Brückner, C. Cramer, C. Krieger, A. Mandanici, C. Martiny, I. Ross, Physical Chemistry Chemical Physics 4 (2002) 3155-3167.
[8] J. Jamnik, J. Maier, S. Pejovnik, Electrochimica Acta 44 (1999) 4139-4145.
[9] I.M. Hodge, M.D. Ingram, A.R. West, Journal of Electroanalytical Chemistry and Interfacial Electrochemistry 74 (1976) 125-143.
[10] J.T.S. Irvine, D.C. Sinclair, A.R. West, Advanced Materials 2 (1990) 132-138.
[11] R.L. Hurt, J.R. Macdonald, Solid State Ionics 20 (1986) 111-124.
[12] J.R. Macdonald, Electrochimica Acta 35 (1990) 1483-1492.
[13] B.A. Boukamp, J. Ross Macdonald, Solid State Ionics 74 (1994) 85-101.
[14] E. Barsoukov, J. Macdonald, Fundamentals of Impedance Spectroscopy, Impedance Spectroscopy, John Wiley & Sons, Inc., 2005.
[15] M. Gerstl, E. Navickas, G. Friedbacher, F. Kubel, M. Ahrens, J. Fleig, Solid State Ionics 185 (2011) 32-41.
[16] C. Peters, A. Weber, B. Butz, D. Gerthsen, E. Ivers-Tiffée, Journal of the American Ceramic Society 92 (2009) 2017-2024.
[17] M. Li, M.J. Pietrowski, R.A. De Souza, H. Zhang, I.M. Reaney, S.N. Cook, J.A. Kilner, D.C. Sinclair, Nature Materials 13 (2014) 31-35.
[18] L. Rioja-Monllor, C. Bernuy-Lopez, M.-L. Fontaine, T. Grande, M.-A. Einarsrud, Journal of Materials Chemistry A 7 (2019) 8609-8619.
[19] G.M. Rupp, A. Schmid, A. Nenning, J. Fleig, Journal of The Electrochemical Society 163 (2016) F564-F573.
[20] A. Schmid, G.M. Rupp, J. Fleig, Physical Chemistry Chemical Physics 20 (2018) 12016-12026.
[21] G.M. Rupp, A.K. Opitz, A. Nenning, A. Limbeck, J. Fleig, Nature Materials 16 (2017) 640-645.

[22] W. Lai, S.M. Haile, Journal of the American Ceramic Society 88 (2005) 2979-2997.
[23] L. Medenbach, C.L. Bender, R. Haas, B. Mogwitz, C. Pompe, P. Adelhelm, D. Schröder, J. Janek, Energy Technology 5 (2017) 2265-2274.
[24] S. Kranz, T. Kranz, T. Graubner, Y. Yusim, L. Hellweg, B. Roling, Batteries & Supercaps 2 (2019) 1026-1036.
[25] A. West, D. Sinclair, N. Hirose, Journal of Electroceramics 1 (1997) 65-71.
[26] Y. Huang, K. Wu, Z. Xing, C. Zhang, X. Hu, P. Guo, J. Zhang, J. Li, Journal of Applied Physics 125 (2019) 084103.
[27] J. Rödel, W. Jo, K.T.P. Seifert, E.-M. Anton, T. Granzow, D. Damjanovic, Journal of the American Ceramic Society 92 (2009) 1153-1177.
[28] J. Koruza, A.J. Bell, T. Frömling, K.G. Webber, K. Wang, J. Rödel, Journal of Materiomics 4 (2018) 13-26.
[29] T. Frömling, S. Steiner, A. Ayrikyan, D. Bremecker, M. Dürrschnabel, L. Molina-Luna, H.-J. Kleebe, H. Hutter, K.G. Webber, M. Acosta, Journal of Materials Chemistry C 6 (2018) 738-744.
[30] S. Steiner, J. Heldt, O. Sobol, W. Unger, T. Frömling, Journal of the American Ceramic Society 104 (2021) 4341-4350.
[31] W. Jo, S. Schaab, E. Sapper, L.A. Schmitt, H.-J. Kleebe, A.J. Bell, J. Rödel, Journal of Applied Physics 110 (2011) 074106.
[32] J. Kling, X. Tan, W. Jo, H.-J. Kleebe, H. Fuess, J. Rödel, Journal of the American Ceramic Society 93 (2010) 2452-2455.
[33] J.E. Daniels, W. Jo, J. Rödel, V. Honkimäki, J.L. Jones, Acta Materialia 58 (2010) 2103-2111.
[34] J. Zang, M. Li, D.C. Sinclair, W. Jo, J. Rödel, Journal of the American Ceramic Society 97 (2014) 1523-1529.
[35] S. Gorfman, P.A. Thomas, Journal of Applied Crystallography 43 (2010) 1409-1414.
[36] L.A. Schmitt, J. Kling, M. Hinterstein, M. Hoelzel, W. Jo, H.J. Kleebe, H. Fuess, Journal of Materials Science 46 (2011) 4368-4376.
[37] J. Zang, M. Li, D.C. Sinclair, T. Frömling, W. Jo, J. Rödel, Journal of the American Ceramic Society 97 (2014) 2825-2831.
[38] M. Acosta, J.D. Zang, W. Jo, J. Rodel, Journal of the European Ceramic Society 32 (2012) 4327-4334.
[39] M. Höfling, S. Steiner, A.-P. Hoang, I.-T. Seo, T. Frömling, Journal of Materials Chemistry C 6 (2018) 4769-4776.
[40] X. Guo, Z. Zhang, W. Sigle, E. Wachsman, R. Waser, Applied Physics Letters 87 (2005) -.
[41] J. East, D.C. Sinclair, Journal of Materials Science Letters 16 (1997) 422-425.
[42] R. Gerhardt, Journal of Physics and Chemistry of Solids 55 (1994) 1491-1506.
[43] R.J. Grant, M.D. Ingram, A.R. West, Electrochimica Acta 22 (1977) 729-734.
[44] D.P. Almond, C.C. Hunter, A.R. West, Journal of Materials Science 19 (1984) 3236-3248.
[45] R.A. Huggins, Ionics 8 (2002) 300-313.
[46] J. Maier, Berichte der Bunsengesellschaft für physikalische Chemie 90 (1986) 26-33.
[47] Y. Liu, Y. Bai, W. Jaegermann, R. Hausbrand, B.-X. Xu, ACS Applied Materials & Interfaces 13 (2021) 5895-5906.
[48] L. Koch, S. Steiner, K.-C. Meyer, I.-T. Seo, K. Albe, T. Frömling, Journal of Materials Chemistry C 5 (2017) 8958-8965.
[49] Q. Xu, M.T. Lanagan, W. Luo, L. Zhang, J. Xie, H. Hao, M. Cao, Z. Yao, H. Liu, Journal of the European Ceramic Society 36 (2016) 2469-2477.
[50] T.J.M. Bayer, J.-J. Wang, J.J. Carter, A. Moballegh, J. Baker, D.L. Irving, E.C. Dickey, L.-Q. Chen, C.A. Randall, Acta Materialia 117 (2016) 252-261.
[51] M. Vögler, N. Novak, F.H. Schader, J. Rödel, Physical Review B 95 (2017) 024104.
[52] M. Acosta, J. Zang, W. Jo, J. Rödel, Journal of the European Ceramic Society 32 (2012) 4327-4334.
[53] M. Acosta, L.A. Schmitt, L. Molina-Luna, M.C. Scherrer, M. Brilz, K.G. Webber, M. Deluca, H.-J. Kleebe, J. Rödel, W. Donner, Journal of the American Ceramic Society 98 (2015) 3405-3422.

[54] J. Koruza, V. Rojas, L. Molina-Luna, U. Kunz, M. Duerrschnabel, H.-J. Kleebe, M. Acosta, Journal of the European Ceramic Society 36 (2016) 1009-1016.
[55] H.-C. Thong, C. Zhao, Z.-X. Zhu, X. Chen, J.-F. Li, K. Wang, Acta Materialia 166 (2019) 551-559.
[56] B. Jaffe, W.R. Cook, H. Jaffe, Piezoelectric Ceramics, Academic Press Inc., 1971, p. 328.

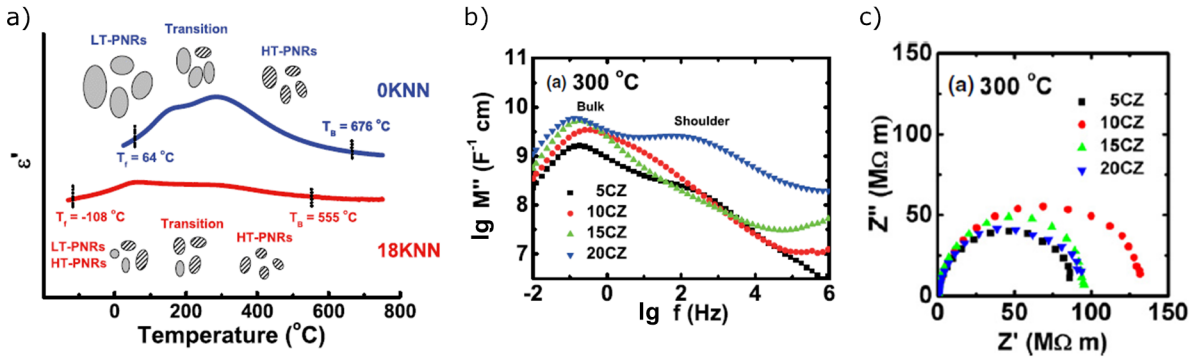

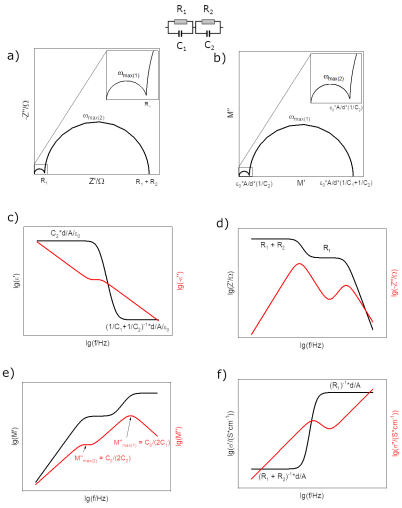

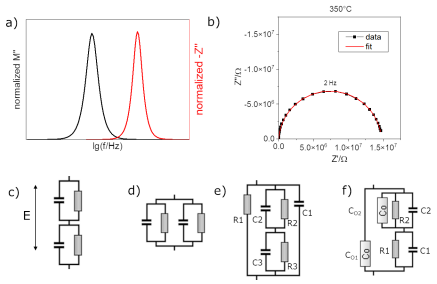

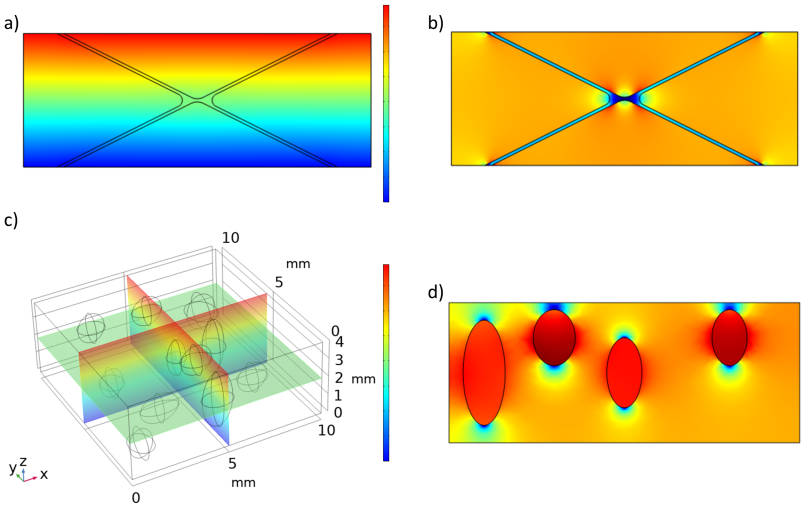

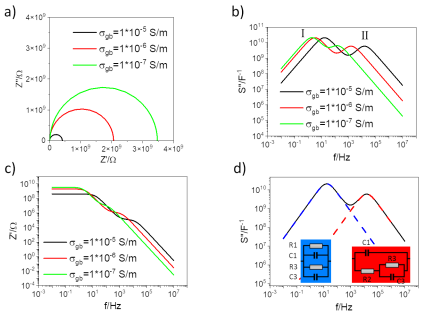

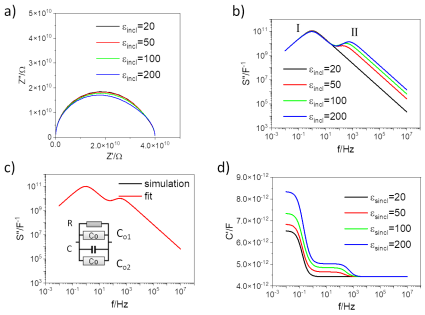

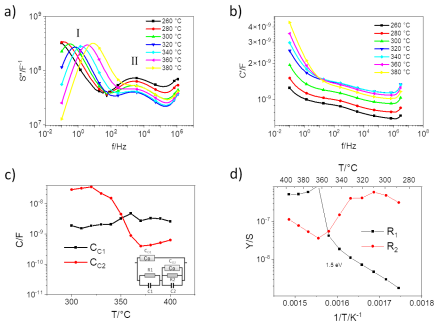

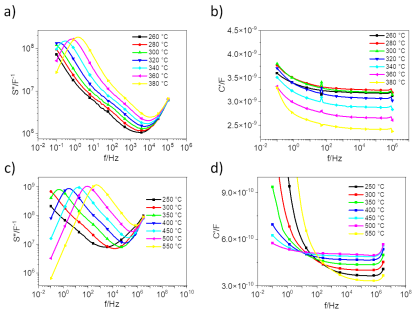

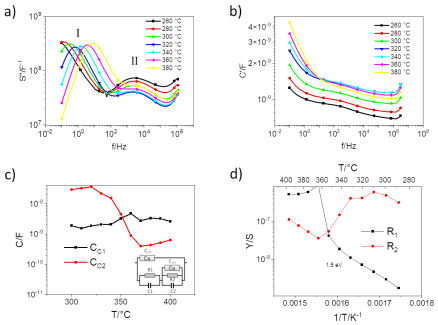

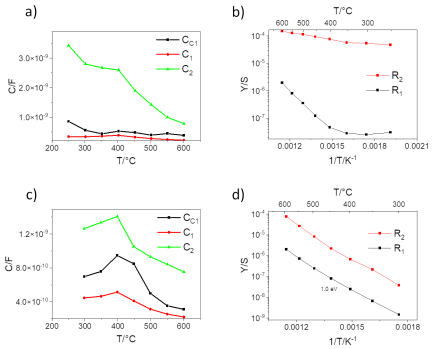

- Analysis of parallel dielectric and conductive pathways is possible via modulus analysis.
- Lead-free dielectrics and ferroelectrics are prone to develop parallel processes due to chemical or structural inhomogeneity.
- The response of different polar nanoregions can be quantified.
- The approach can be applied to any dielectric or electrically conducting material.

Conflict of interest

Authors declare that there are no conflicts of interest.

Till Frömling graduated in chemistry from the Philipps-University of Marburg, Germany. He then went to pursue a Ph.D. at the Technical University of Vienna. After completion of his Ph.D. in 2011 he joined SB Limotive/Bosch Battery Systems working on the development of energy storage systems. Since the end of 2013 he is a group leader at the Technische Universität Darmstadt, Germany. His research focuses on the defect chemistry of lead-free ferroelectrics and the mechanical modification of ionic and electronic conductivity of oxides.

Associate Professor Julia Glaum is a group leader in the Functional Materials and Materials Chemistry (FACET) group at the Norwegian University of Science and Technology (NTNU), Norway. Her main research interests focus on the applicability of functional materials for biomedical applications, including various aspects from processing and functionality optimization to reliability studies and regulation compliance. She has been the principle investigator of projects funded by the Norwegian and the Australian Research Council as well as the European Commission.

Bai-Xiang Xu, professor, leader of the Division Mechanics of Functional Materials, Institute of Materials Science, Technische Universität Darmstadt, Germany. She received her Ph.D. Degree in solid mechanics from Peking University, Beijing in 2008, and afterwards she was rewarded with the Alexander von Humboldt Postdoctoral Scholarship. In 2011 she joined the Technische Universität Darmstadt as a faculty and had been chairing the division ever since. Her current research topics include description and optimization of microstructure and the related mechanical and functional properties in functional and energy materials by multiphysics models and numerical simulations, particularly phase-field approach, micromechanics theory, and finite element methods.

Till Frömling

Julia Glaum

Bai-Xiang Xu